Contactless pick-and-place of millimetric objects using inverted near-field acoustic levitation

Marco A. B. Andrade[1,a)], Tiago S. Ramos[2], Julio C. Adamowski[3], and Asier Marzo[4]

[1]*Instituto de Física, Universidade de São Paulo, São Paulo 05508-090, Brazil*
[2]*Physics Department, University of Massachusetts, Amherst, MA 01003, USA*
[3]*Escola Politécnica, Universidade de São Paulo, São Paulo 05508-030, Brazil*
[4]*UpnaLab, Universidad Pública de Navarra, Pamplona 31006, Navarra, Spain*

Abstract: We model and realize an ultrasonic contactless pick-and-place device capable of picking, self-centering, self-orienting, translating and releasing flat millimetric objects. The device is an ultrasonic Langevin transducer operating at 21 kHz that radiates into air through a tapered tip. Objects are trapped few micrometers below the tip due to the near-field acoustic levitation phenomenon. We firstly investigate the conditions to achieve an attractive force on the object depending on its size and the device operating frequency. Secondly, we use a 3D acoustic model that describes the converging forces and torque that provide the self-centering and self-orienting capabilities. Thirdly, a more advanced Computational Fluid Dynamics (CFD) model based on the Navier-Stokes equations explains the small gap between the tip and the trapped object. The contactless manipulation capabilities of the device are demonstrated by picking, transporting and releasing a Surface Mount Device (SMD) in air. The presented manipulation concept can be an interesting alternative for manipulating delicate objects such as microelectromechanical devices, silicon dies or micro-optical devices.

[a)]Author to whom correspondence should be addressed. Electronic mail: marcobrizzotti@gmail.com

Handling small components is crucial in microelectronics[1] and in the assembly of microelectromechanical systems (MEMS)[2]. Gravity and inertial forces play a major role in the manipulation of large objects; in contrast, the manipulation of small components is dominated by surface forces (e.g. electrostatic and van Der Waals)[3,4]. Surface forces can produce undesired adhesion between the small objects and the grippers, preventing the accurate release of the objects. In addition, the contact with the gripper can cause contamination or damage fragile components.

To avoid the issues caused by the contact between the gripper and the object, methods such as magnetic[5], optical[6], aerodynamic[7,8] or acoustophoretic[9] noncontact handling are employed. Among these methods, acoustic levitation has the main advantage of being able to manipulate a wide range of materials, including solids[10,11], liquids[12–14] and even living creatures[15]. Furthermore, it can work at scales varying from micrometers[16] up to centimeters[11,17,18].

Different acoustic levitation approaches have been used for manipulating objects[9]. The most commonly used method traps small objects at the pressure nodes of a standing wave field[10,19–22]. This technique also allows the manipulation of the levitated object by controlling the sound field generated by multiple emitters[23–25]. Despite the flexibility of acoustic levitators, contact methods such as tweezers are often required to insert the object into the levitator. Furthermore, undesired oscillations[26,27] can hinder its use in the precise manipulation of objects.

Another acoustic method for suspending objects in midair is near-field acoustic levitation[28,29], in which large planar objects are suspended tens of micrometers above a vibrating surface. It has been reported that there are cases in which the radiation force exerted on an object changes from repulsive to attractive, allowing the suspension of small objects slightly below the transducer vibrating surface[30–33]. However, it is not clear what are the conditions to obtain an attractive or repulsive force using near-field acoustic levitation or what are the forces and torques that this phenomenon exerts on the objects. An attractive near-field acoustic levitator (i.e. inverted near-field acoustic levitator) could be of interest for pick-and-place applications since it can grip objects by just accessing their top surface.

In this letter, we first model the near-field acoustic levitation phenomenon for determining the conditions that lead to an attractive force on the levitated object. Based on this analysis, we develop an attractive near-field acoustic levitator for the pick-and-place of millimetric scale components. In this inverted near-field acoustic levitator,

millimetric components are acoustically suspended slightly below a transducer tip vibrating at 21 kHz. The noncontact forces and torques acting on the object are also calculated by a 3D acoustic model and a 2D axisymmetric Computational Fluid Dynamics (CFD) simulation.

We start our study by performing acoustic simulations based on the Finite Element Method (FEM) to find the conditions that lead to an attractive or repulsive force on an object. A 2D axisymmetric acoustic model is implemented in the software COMSOL Multiphysics for calculating the acoustic radiation force acting on a circular object of radius R. The sound wave is emitted by a circular surface, also with radius R, and with a separation H from the object [Fig. 1(a)]. The transducer radiating surface vibrates uniformly with velocity amplitude u_t and frequency f. Perfectly Matched Layers (PML) are employed at the edges of the domain to avoid wave reflections. The FEM model is used for obtaining the acoustic pressure p and velocity $\mathbf{u}$ fields in the air domain. Using these fields, the time-averaged acoustic radiation pressure p^{rad} on the object upper surface is calculated by[9,34]

$$p^{rad} = \frac{\langle p^2 \rangle}{2\rho_0 c_0^2} - \frac{\rho_0 \langle \mathbf{u}\cdot\mathbf{u} \rangle}{2}, \tag{1}$$

where ρ_0 = 1.2 kg/m^3 is the air density and c_0 = 343 m/s is the sound velocity in air. Finally, the radiation force acting on the object is determined by[9]

$$\mathbf{F^{rad}} = -\int_{S_0} p^{rad}\mathbf{n}dS. \tag{2}$$

In Eq. (2), $\mathbf{n}$ is the surface normal vector pointing outwards from the object and the integral is evaluated over the top surface (S_0) of the object. To simplify the analysis, we adopt the following dimensionless quantities: $\tilde{p} = p/\rho_0 c_0 u_t$, $\tilde{p}^{rad} = p^{rad}/\rho_0 u_t^2$, $\tilde{\mathbf{u}} = \mathbf{u}/u_t$ and $\tilde{\mathbf{F}}^{\mathbf{rad}} = \mathbf{F}^{\mathbf{rad}}/S_0\rho_0 u_t^2$, with $S_0 = \pi R^2$.

Using the numerical model of Fig. 1(a), the dimensionless acoustic radiation force $\tilde{\mathbf{F}}^{\mathbf{rad}}$ on a circular object was simulated with different values for H/λ and R/λ, where $\lambda = c_0/f$ is the acoustic wavelength. As shown in Fig. 1(b), the radiation force is attractive for $R/\lambda < 0.38$ and repulsive for $R/\lambda > 0.38$. The transition from attractive to repulsive force is indicated by the horizontal dashed line of Fig. 1(b). Figure 1(c) shows the dimensionless force as a function of H/λ for one case in which the force is attractive ($R/\lambda = 0.3$) and another case in which it is repulsive ($R/\lambda = 0.5$). To understand why

the force on the object can be either attractive or repulsive, we plot in Fig. 1(d) the dimensionless radiation pressure $\tilde{p}_{rad}$ acting on the object's top surface for $R/\lambda = 0.3$ and $R/\lambda = 0.5$. In both cases, the distance between the transducer and the reflector is $H/\lambda = 0.5 \times 10^{-3}$. By analyzing the results of Fig. 1(d), one can observe that the radiation pressure is positive on the central region of the object and negative on the region close to the outer rim. For $R/\lambda = 0.5$, the positive radiation pressure dominates and the total force on the object is repulsive; whereas for $R/\lambda = 0.3$, the negative radiation pressure close to the outer rim dominates, leading to an attractive force.

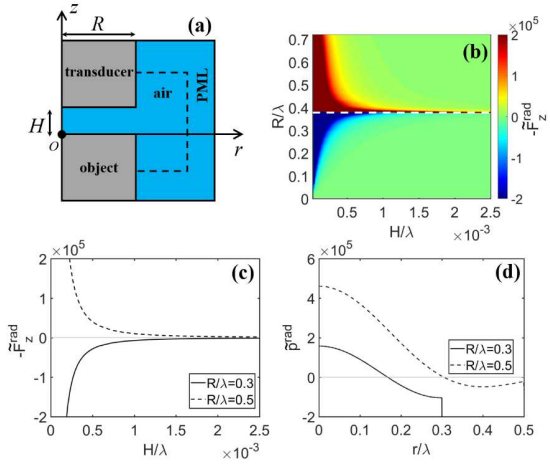

FIG. 1. (a) Axisymmetric acoustic model. (b) Dimensionless force on the object as a function of H/λ and R/λ. (c) Dimensionless force on the object as a function of H/λ for both $R/\lambda = 0.3$ and $R/\lambda = 0.5$. (d) Dimensionless pressure along the object surface for $H/\lambda = 0.5 \times 10^{-3}$.

After determining the condition that results in an attractive force, we design an acoustic levitation device for pick and place small electronic components. Our system should trap a Surface Mount Device (SMD) with lateral dimensions of 1.6 mm x 3.2 mm, a height of 0.55 mm and mass of 9 mg. Based on this component size, we designed a bolt-clamped Langevin transducer[35] with a resonance frequency of 21 kHz (see supplementary material for details on the transducer design). This frequency was chosen because it is above human hearing range and meets the condition for obtaining an attractive force on a SMD component, i.e. $R/\lambda < 0.38$. The simulated displacement amplitude is presented in Fig. 2(a) and a picture of the assembled transducer is shown in Fig. 2(b). The maximum

displacement occurs at the transducer tip, which has a rectangular shape with the same lateral dimensions as the SMD. The manipulation capabilities of the transducer were tested by picking, transporting and releasing SMD components [see Fig. 2 (Multimedia view)].

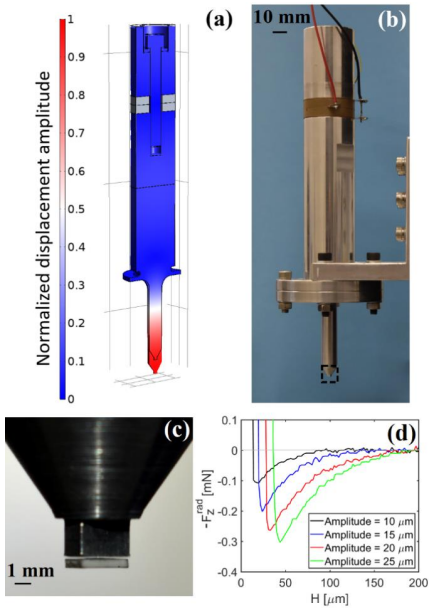

FIG. 2. (a) Simulated displacement amplitude of the transducer at 21 kHz. (b) Picture of the designed transducer. (c) Levitation of a SMD weighting 9 mg. (d) Experimental acoustic radiation force acting on the SMD component as a function of H for various displacement amplitudes of the tip. A video demonstrating the contactless picking, transporting and releasing of SMD components is available online (Multimedia view).

To measure the vertical force acting on the SMD, the transducer was mounted on a motorized translation stage (Thorlabs NRT150/M). The SMD was fixed with double-sided tape to the tray of a scale (Shimadzu UX420H) with a resolution of 1 mg. The force acting on the SMD was measured as a function of H for various displacement amplitudes of the transducer tip [Fig. 2(d)]. In these measurements, H was incremented in steps of 2 µm with an accuracy of approximately ±10 µm. As shown in Fig. 2(d), the radiation force acting on the object is repulsive (i.e. positive) for small values of H and it changes to attractive (i.e. negative) when H reaches a certain distance. The transition separation H from repulsive to attractive depends on the transducer displacement amplitude. In our

experiments, the transition occurred at $H = 15$ μm for a transducer displacement amplitude of 10 μm, and at $H = 35$ μm for a displacement amplitude of 25 μm. This sign transition implies that the vertical force is converging and explains why the object gets trapped below the transducer tip without touching the transducer surface.

In the experiments, we observed that the ultrasonic wave emitted by the transducer tip generates not only a vertical attractive force that suspends the object but also produces a self-centering and self-orientation effect on the levitated object, i.e. the torque and forces are converging. To analyze this position and orientation trapping capability, a 3D acoustic simulation in COMSOL was employed. In this 3D model [Fig. 3(a)], the transducer tip (lateral dimensions of 1.6 mm by 3.2 mm) vibrates harmonically at a frequency of 21 kHz with a displacement amplitude of 10 μm. Similar to the model of Fig. 1(a), this model calculates the acoustic pressure and velocity fields in the air medium surrounding the SMD. These fields are used in Eq. (2) for calculating the acoustic radiation force acting on the trapped object, and the acoustic radiation torque as a function of its orientation angle θ is calculated by[36]

$$\boldsymbol{\tau}^{\mathbf{rad}} = -\int_{S_0} p^{rad}\mathbf{r} \times \mathbf{n} dS, \tag{3}$$

where $\mathbf{r}$ is the vector that points from the center of mass of the SMD to its surface and the integral is evaluated over the object surface S_0.

The simulated acoustic pressure generated by the inverted near-field acoustic levitator is shown in Fig. 3(d). The horizontal stability of the object (i.e. self-centering capability) was analyzed by calculating the horizontal components F_x^{rad} and F_y^{rad} of the acoustic radiation force as a function of the object displacement along the x and y directions. As shown in Figs. 3(b) and 3(c), both F_x^{rad} and F_y^{rad} are positive when the position is negative and negative when the position is positive, i.e. the forces are converging towards an equilibrium point, which provides lateral stability and self-centers the object. The simulated radiation torque for the object rotation around the z-axis [Fig. 3(f)] is also converging, providing orientation stability and self-orients the SMD.

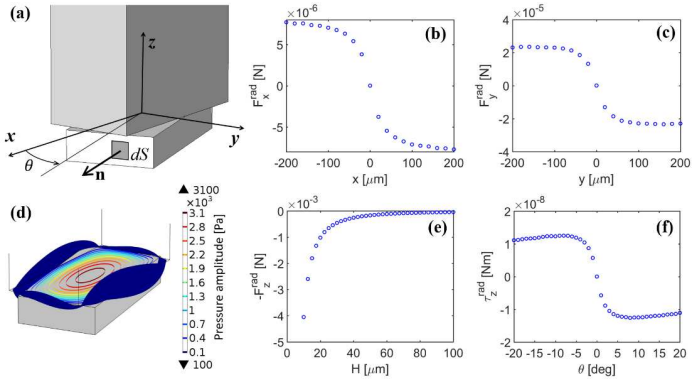

FIG. 3. Simulation of the acoustic radiation force and radiation torque on the SMD component. (a) 3D acoustic model. (b) Force along the x direction. (c) Force along the y direction. (d) Acoustic pressure distribution for $\theta = 10^o$. (e) Vertical acoustic radiation force as a function of H. (f) Radiation torque as a function of the object orientation along the z-axis. The results of Figs. (b), (c), (d) and (f) were obtained for $H = 20$ µm.

The simulated vertical radiation force on the SMD as a function of H is shown in Fig. 3(e). As expected, the 3D acoustic model predicts an attractive vertical force on the object. However, the predicted vertical force is always attractive, even for small values of H. This is in stark contrast with the experimental results of Fig. 2(d), which shows a transition from attractive to repulsive. If the vertical force was always attractive, the SMD would touch the transducer tip, which clearly contradicts Fig. 2(c). The transition from attractive to repulsive force cannot be predicted by the acoustic model of Figs. 1(a) and 3(a). The acoustic model assumes an inviscid medium and it is valid for H much greater than the viscous penetration depth $\delta = \sqrt{2\eta/\rho_0\omega}$ (where η = 1.81 x 10^{-5} Pa.s is the air dynamic viscosity). In our experiments, $\delta \approx 15$ µm and the transition from repulsive to attractive force occurred for H varying between 15 and 35 µm. This suggests that the air viscosity affects the flow between the transducer and the object and needs to be considered for small values of H (see supplementary material for details on the effect of air viscosity).

To take into account air viscosity, a CFD model based on the Navier-Stokes equations was implemented in COMSOL to simulate the force on the object for different values of H (see supplementary material for more details on the CFD model). In the CFD simulations, the transducer displacement amplitude was set to 10 µm. To reduce the computational cost, the force on the object was simulated using an axisymmetric CFD

model with both the transducer tip and the object having a radius of 1.27 mm. This radius was obtained by assuming that the object has the same area as a SMD component of lateral dimensions 1.6 mm x 3.2 mm.

The simulated force on the object over time for a separation $H = 50$ µm is shown in Fig. 4(a). The negative peaks are larger than the positive peaks, which causes the time-averaged force on the object to be attractive for $H = 50$ µm. Figure 4(b) shows the comparison between the time-averaged force acting on the object obtained both with the CFD model and with an axisymmetric acoustic model. As shown in Fig. 4(b), there is a good agreement between the two curves for $H > 75$ µm. For $H \approx 30$ µm, only the CFD model predicts a transition from a repulsive to an attractive force, which is in qualitative agreement with the experimental force on the SMD component shown in Fig. 2(d) (see supplementary material for details on the qualitative agreement).

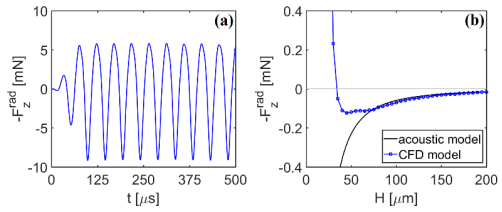

FIG. 4. Simulated vertical force on a circular object of radius $R = 1.27$ mm for a transducer displacement amplitude of 10 µm. (a) Force on the object over time using the CFD model for $H = 50$ µm. (b) Time-averaged vertical force on the object as a function of H obtained both with the CFD model and with the acoustic model.

To summarize, we have investigated the near-field acoustic levitation technique and found that the radiation force on the object is attractive if $R/\lambda < 0.38$ and repulsive if $R/\lambda > 0.38$. Based on this analysis, we designed an inverted near-field acoustic levitation device for the contactless picking, transporting and releasing of SMD components. The position and orientation stability of the device was also analyzed by a 3D acoustic model. A more advanced axisymmetric CFD model was used to capture the transition from an attractive to a repulsive vertical force when the object gets closer to the vibrating tip. The presented pick-and-place device was designed for trapping flat components with the same lateral dimensions as its radiating tip. However, this device could also be used to levitate objects with other shapes and sizes (see supplementary material for an example). Future studies could study the effect on force and torque of

lateral dimensions and shape mismatch between the radiating tip and the object. Inverted near-field acoustic levitation extends the capabilities of the current acoustic levitation devices by enabling to pick, transport and release delicate objects. The device only needs access to the top surface and provides a contactless, self-centering, self-oriented and non-electrostatic way of handling small objects.

See the supplementary material for more details on: the transducer design and fabrication, the CFD simulations, experimental and simulated vertical forces, effect of air viscosity, and trapping of a non-flat object.

This research was supported by the São Paulo Research Foundation – FAPESP (Grants Nos. 2017/27078-0 and 2018/04101-0).

[1] M.R. Marks, Z. Hassan, and K.Y. Cheong, Crit. Rev. Solid State Mater. Sci. **40**, 251 (2015).
[2] K. Tsui, A.A. Geisberger, M. Ellis, and G.D. Skidmore, J. Micromechanics Microengineering **14**, 542 (2004).
[3] R.S. Fearing, in *Proc. 1995 IEEE/RSJ Int. Conf. Intell. Robot. Syst.* (1995), pp. 212–217.
[4] V. Vandaele, P. Lambert, and A. Delchambre, Precis. Eng. **29**, 491 (2005).
[5] B.Z. Kaplan, Proc. Inst. Electr. Eng. **114**, 1801 (1967).
[6] D.G. Grier, Nature **424**, 810 (2003).
[7] J.A. Paivanas and J.K. Hassan, IBM J. Res. Dev. **23**, 361 (1979).
[8] K. Shi and X. Li, Exp. Therm. Fluid Sci. **77**, 284 (2016).
[9] M.A.B. Andrade, N. Pérez, and J.C. Adamowski, Brazilian J. Phys. **48**, 190 (2018).
[10] W.J. Xie and B. Wei, Appl. Phys. Lett. **79**, 881 (2001).
[11] M.A.B. Andrade, A.L. Bernassau, and J.C. Adamowski, Appl. Phys. Lett. **109**, 044101 (2016).
[12] D. Foresti, M. Nabavi, M. Klingauf, A. Ferrari, and D. Poulikakos, Proc. Natl. Acad. Sci. **110**, 12549 (2013).
[13] M.A.B. Andrade, T.S.A. Camargo, and A. Marzo, Rev. Sci. Instrum. **89**, 125105 (2018).
[14] S. Tsujino and T. Tomizaki, Sci. Rep. **6**, 25558 (2016).
[15] W.J. Xie, C.D. Cao, Y.J. Lü, Z.Y. Hong, and B. Wei, Appl. Phys. Lett. **89**, 214102 (2006).
[16] C. Devendran, D.R. Billson, D.A. Hutchins, and A. Neild, Sensors Actuators, B Chem. **224**, 529 (2016).
[17] A. Marzo, M. Caleap, and B.W. Drinkwater, Phys. Rev. Lett. **120**, 44301 (2018).
[18] S. Inoue, S. Mogami, T. Ichiyama, A. Noda, Y. Makino, and H. Shinoda, J. Acoust. Soc. Am. **145**, 328 (2019).
[19] J.K.R. Weber, C.A. Rey, J. Neuefeind, and C.J. Benmore, Rev. Sci. Instrum. **80**, 083904 (2009).
[20] M.A.B. Andrade, N. Pérez, and J.C. Adamowski, Appl. Phys. Lett. **106**, 014101 (2015).
[21] L. Cox, A. Croxford, B.W. Drinkwater, and A. Marzo, Appl. Phys. Lett. **113**, 054101

(2018).
[22] D. Koyama and K. Nakamura, IEEE Trans. Ultrason. Ferroelectr. Freq. Control **57**, 1152 (2010).
[23] Y. Ochiai, T. Hoshi, and J. Rekimoto, PLoS One **9**, e97590 (2014).
[24] A. Marzo, S.A. Seah, B.W. Drinkwater, D.R. Sahoo, B. Long, and S. Subramanian, Nat. Commun. **6**, 8661 (2015).
[25] A. Marzo and B.W. Drinkwater, Proc. Natl. Acad. Sci. **116**, 84 (2019).
[26] M.A.B. Andrade, N. Pérez, and J.C. Adamowski, J. Acoust. Soc. Am. **136**, 1518 (2014).
[27] S. Tsujino, Y. Sato, Y. Takeda, and T. Tomizaki, Appl. Phys. Lett. **115**, 053702 (2019).
[28] S. Ueha, Y. Hashimoto, and Y. Koike, Ultrasonics **38**, 26 (2000).
[29] Y. Hashimoto, Y. Koike, and S. Ueha, J. Acoust. Soc. Am. **100**, 2057 (1996).
[30] M. Takasaki, D. Terada, Y. Kato, Y. Ishino, and T. Mizuno, Phys. Procedia **3**, 1059 (2010).
[31] S. Yoshimoto, T. Shou, and K. Somaya, Precis. Eng. **37**, 805 (2013).
[32] M. Takasaki, S. Chino, Y. Kato, Y. Ishino, and T. Mizuno, Key Eng. Mater. **523**–**524**, 727 (2012).
[33] T. Hatanaka, Y. Koike, K. Nakamura, S. Ueha, and Y. Hashimoto, Japanese J. Appl. Physics, Part 2 Lett. **38**, L1284 (1999).
[34] Z.Y. Hong, W. Zhai, N. Yan, and B. Wei, J. Acoust. Soc. Am. **135**, 2553 (2014).
[35] J.A. Gallego-Juarez, J. Phys. E Sci. Instrum. **22**, 804 (1989).
[36] T. Schwarz, P. Hahn, G. Petit-Pierre, and J. Dual, Microfluid. Nanofluidics **18**, 65 (2014).

SUPPLEMENTARY MATERIAL

Contactless pick-and-place of millimetric objects using inverted near-field acoustic levitation

Marco A. B. Andrade[1], Tiago S. Ramos[2], Julio C. Adamowski[3], and Asier Marzo[4]

AFFILIATIONS

[1]Instituto de Física, Universidade de São Paulo, São Paulo 05508-090, Brazil
[2]Physics Department, University of Massachusetts, Amherst, MA 01003, USA
[3]Escola Politécnica, Universidade de São Paulo, São Paulo 05508-030, Brazil
[4]UpnaLab, Universidad Pública de Navarra, Pamplona 31006, Navarra, Spain

S1. Design and fabrication of the Langevin transducer

The contactless manipulation of SMD components is performed with a bolt-clamped Langevin type transducer, which was specially designed for this task. The Langevin type transducer consists of a sandwich structure and a mechanical amplifier, as illustrated in Fig. S1. The sandwich structure is formed by two piezoelectric rings, which are compressed between two aluminum blocks by a central bolt. The mechanical amplifier basically consists of two aluminum cylindrical blocks of different diameters. When a sinusoidal electric signal is applied at the electrodes of the piezoelectric rings, the sandwich structure vibrates as a half-wavelength resonator. The axial vibration generated by the sandwich structure is amplified by the mechanical amplifier, allowing high displacement amplitudes at the transducer tip. The mechanical amplifier also works as a half-wavelength resonator. The axial displacement profile along the transducer is shown in Fig. S1.

The transducer was designed to operate at 21 kHz. This frequency was chosen because it is above the range of human hearing and it meets the condition for obtaining an attractive force on the target object (i.e. $R/\lambda < 0.38$). The transducer is simulated and designed using the Finite Element Method (FEM) software COMSOL Multiphysics. The

transducer design is carried out in two steps. First, the sandwich structure is simulated using an axisymmetric FEM model and its geometric parameters are manually adjusted until the sandwich structure resonates at the desired frequency (i.e. 21 kHz). Then another model is used to simulate and design the mechanical amplifier.

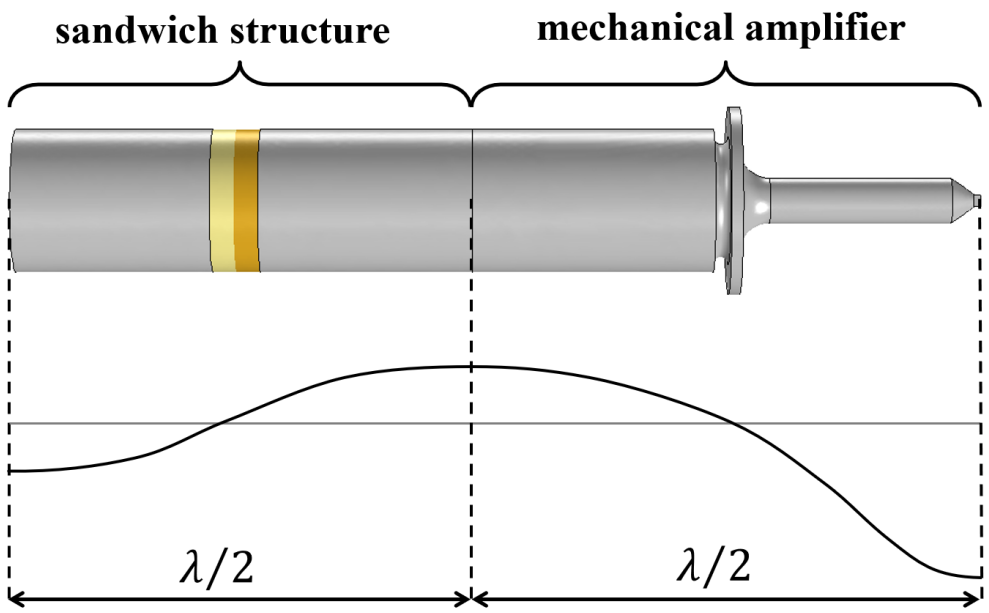

FIG. S1. Langevin type transducer consisting of two main parts: a sandwich structure and a mechanical amplifier. Each part operates as a half-wavelength resonator, as illustrated in the axial displacement profile.

The FEM model used for designing the sandwich structure is shown in Fig. S2. The sandwich structure consists of two piezoelectric rings made of Lead Titanate Zirconate (PZT-4) of 38.1 mm external diameter, 12.7 mm internal diameter and 6.35 mm thickness, which are compressed between two aluminum cylindrical blocks by a M10 allen steel bolt. The sandwich structure is illustrated in Fig. S2(a) and its axisymmetric FEM model with the geometric parameters is shown in Fig. S2(b). The aluminum blocks, the steel bolt and the washer were modeled using linear elastic solids elements whereas the piezoelectric rings were modeled using piezoelectric elements. The material properties used in the FEM simulations are presented in Table S1. In the material properties of PZT-4, ρ is the density, C_{ij}^{E} are the stiffness constants at constant electric field, e_{ij} are the piezoelectric constants, and $\varepsilon_{ij}^{S}/\varepsilon_0$ are the dielectric constants, where ε_0 = 8.85 x 10^{-12} F/m is the permittivity of free space. For the aluminum and steel parts, E is the Young's modulus and ν is the Poisson's ratio.

As a starting point, the total length (L) was estimated by approximating the sandwich structure by an aluminum cylindrical bar with a diameter much smaller than its length. For the bar vibrating in its first extensional mode, the total length L is given by:

$$L = \frac{1}{2f}\sqrt{\frac{E}{\rho}}, \tag{S1}$$

where f = 21 kHz is the desired frequency, E = 7 x 10^{10} N/m^2 is the aluminum Young's Modulus and ρ = 2700 kg/m^3 is the aluminum density. Then, by carrying out FEM simulations in the frequency domain, the geometric parameters of Fig. S2(b) were adjusted until the resonance frequency matched the desired frequency of 21 kHz. The final geometric parameters of the sandwich structure after this adjustment process are presented in Table S2. The simulated vibration of the sandwich structure at 21 kHz is shown in Fig. S2(c).

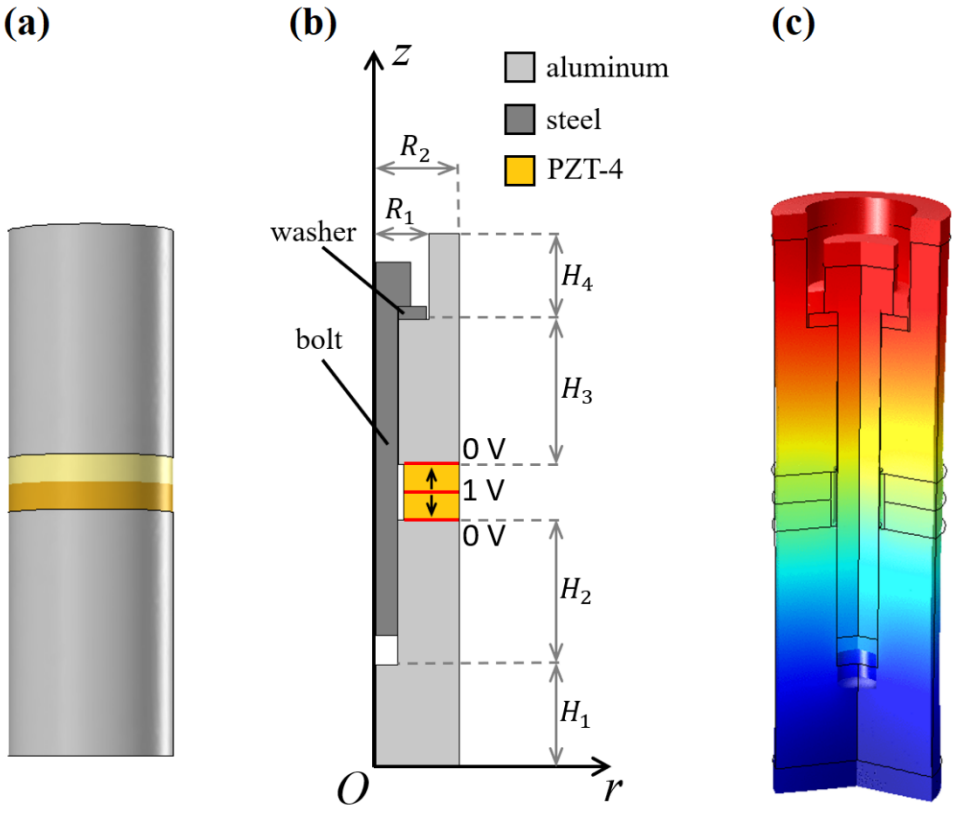

FIG. S2. Simulation and design of the sandwich structure consisting of two piezoelectric rings and two cylindrical blocks. (a) Illustration of the bolt-clamped sandwich structure. (b) Axisymmetric FEM model with its geometrical parameters. (c) Simulated vibration of the sandwich structure at 21 kHz.

TABLE S1. Material properties.

PZT-4	
C_{11}^E (10^{10} N/m^2)	13.90
C_{12}^E (10^{10} N/m^2)	7.78
C_{13}^E (10^{10} N/m^2)	7.43
C_{33}^E (10^{10} N/m^2)	11.54
C_{44}^E (10^{10} N/m^2)	2.56
e_{31} (C/m^2)	-5.20
e_{33} (C/m^2)	15.08
e_{15} (C/m^2)	12.72
$\varepsilon_{11}^S/\varepsilon_0$	762.5
$\varepsilon_{33}^S/\varepsilon_0$	663.2
ρ (kg/m^3)	7500
Aluminum	
E (10^{10} N/m^2)	7.0
ν	0.33
ρ (kg/m^3)	2700
Steel	
E (10^{10} N/m^2)	20
ν	0.33
ρ (kg/m^3)	7850

The mechanical amplifier of the transducer is simulated and designed by carrying out 3D simulations in COMSOL. The FEM model of the mechanical amplifier is shown in Fig. S3(a). The transducer has a rectangular tip with the same lateral dimensions as the SMD resistor (1.6 mm x 3.2 mm). By conducting an Eigenfrequency analysis in COMSOL, the geometric parameters of the mechanical amplifier are adjusted until it resonates at the desired frequency. In this adjustment process, the parameters H_5 and H_7 were carefully adjusted in order to make the amplifier resonate at 21 kHz while reducing the mechanical vibration at the supporting flange located at the middle of the mechanical amplifier. The final geometric parameters after this adjustment process is presented in Table S2. The simulated vibration of the mechanical amplifier at 21 kHz is shown in Fig. S3(b). As shown in this figure, the mechanical amplifier has a low axial displacement on the top and a high displacement amplitude at the transducer tip.

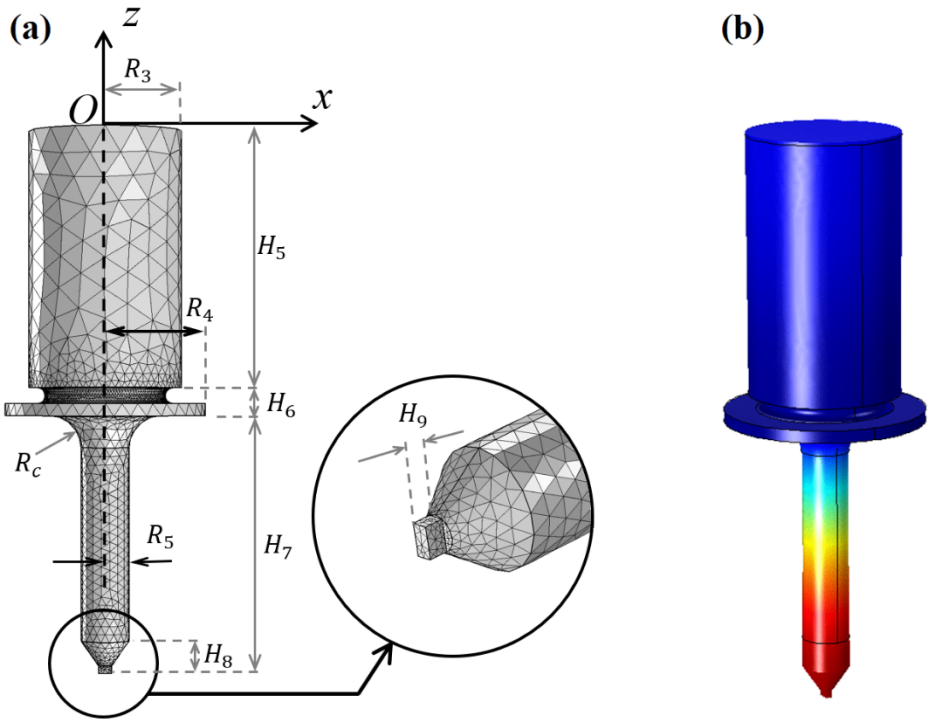

FIG. S3. Simulation and design of the mechanical amplifier. (a) 3D FEM model of the mechanical amplifier. (b) Simulated vibration at 21 kHz.

TABLE S2. Transducer geometric parameters.

Sandwich structure	
H_1	23.5 mm
H_2	33.0 mm
H_3	33.0 mm
H_4	19.5 mm
R_1	12.0 mm
R_2	19.05 mm
Mechanical amplifier	
H_5	64.0 mm
H_6	7.0 mm
H_7	64.3 mm
H_8	8.0 mm
H_9	2.0 mm
R_3	19.05 mm
R_4	25.0 mm
R_5	6.0 mm
R_c	8.0 mm

After designing the sandwich structure and the mechanical amplifier separately, both parts are coupled together and the whole transducer is simulated. The simulated vibration of the transducer at 21 kHz is shown in Fig. S4(a). As shown in Fig. S4(a), when a voltage amplitude of 1 V is applied at the electrodes of the piezoelectric ceramics, the transducer vibrates, generating a large displacement amplitude on the transducer tip.

Using the geometric parameters of Table S2, the parts were machined and the transducer was assembled. To assemble the transducer, a torque wrench was used to apply a torque of 50 Nm to the clamping bolt. A picture of the assembled transducer is shown in Fig. S4(b).

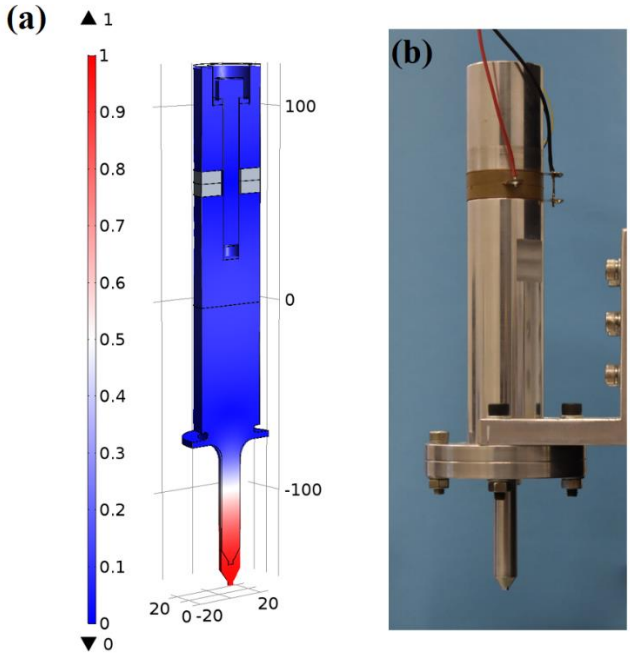

FIG. S4. Langevin type transducer designed for the contactless pick-and-place of SMD components. (a) Simulated vibration at 21 kHz. (b) Picture of the transducer.

S2. Computational Fluid Dynamics (CFD) model

The CFD simulations of the inverted near-field acoustic levitation device were carried out using the Fluid-Structure Interaction (FSI) interface of COMSOL Multiphysics. The axisymmetric CFD model is shown in Fig. S5. An Arbitrary Lagrangian-Eulerian (ALE) formulation was used to model the displacement of the transducer surface located at a mean distance H above the object surface. The object surface ($z = 0$, $0 \leq r \leq 1.27$ mm) was modeled as a rigid wall ($\mathbf{u} = 0$) and the transducer surface was modeled by assuming that its vertical velocity is given by:

$$u_z(t) = A\omega sin(\omega t) step(t), \tag{S3}$$

where A = 10 μm is the displacement amplitude, $\omega = 2\pi f$ is the angular frequency, where f = 21 kHz, and the step function $step(t)$ changes from 0 to 1 in approximately 100 μs.

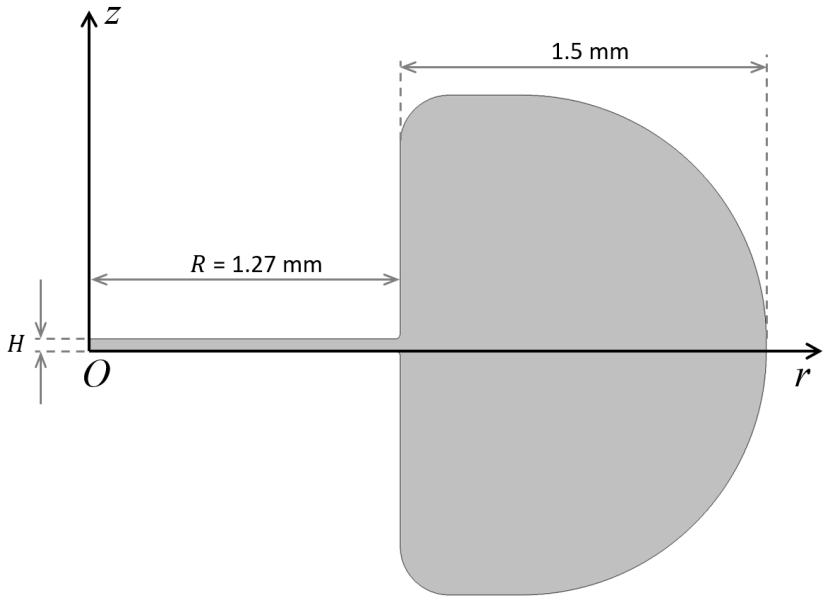

FIG. S5. Computational Fluid Dynamics (CFD) model of the inverted near field acoustic levitation device.

The air medium is modeled using an adiabatic equation of state given by

$$\rho = \rho_0 \left[\frac{p+p_0}{p_0}\right]^{1/\gamma}, \tag{S2}$$

where ρ_0 = 1.2 kg/m^3 is the density of the unperturbed medium, p_0 = 1.01 x 10^5 Pa is the atmospheric pressure and γ = 1.4 is the ratio of specific heats. In addition, it was considered an air dynamic viscosity of 1. 81 x 10^{-5} Pa.s. The simulations were carried out with H varying from 20 μm to 200 μm. For each simulation, the time varied between t = 0 to t = 500 μs.

The CFD simulations simulated the pressure and velocity fields in the air domain as a function of time. A typical simulation result is presented in Fig. S6, which shows the velocity [Figs. S6(a) and S6(b)] and pressure [Fig. S6(c)] fields at t = 408 μs in a simulation with H = 50 μm. To obtain the force on the object, the simulated stress tensor was integrated over the object surface to find the vertical force on the object over time [Fig. S6(d)]. As we can see, although the transducer vibrates sinusoidally, the nonlinearity

of the Navier-Stokes equations causes a non-sinusoidal force on the object surface, whose time-average is nonzero. To find the force on the object, we calculate the time-average force along four periods of the force curve shown in Fig. S6(d). For this particular case, the average vertical force is -11.9 x 10^{-5} N, which corresponds to an attractive force on the object.

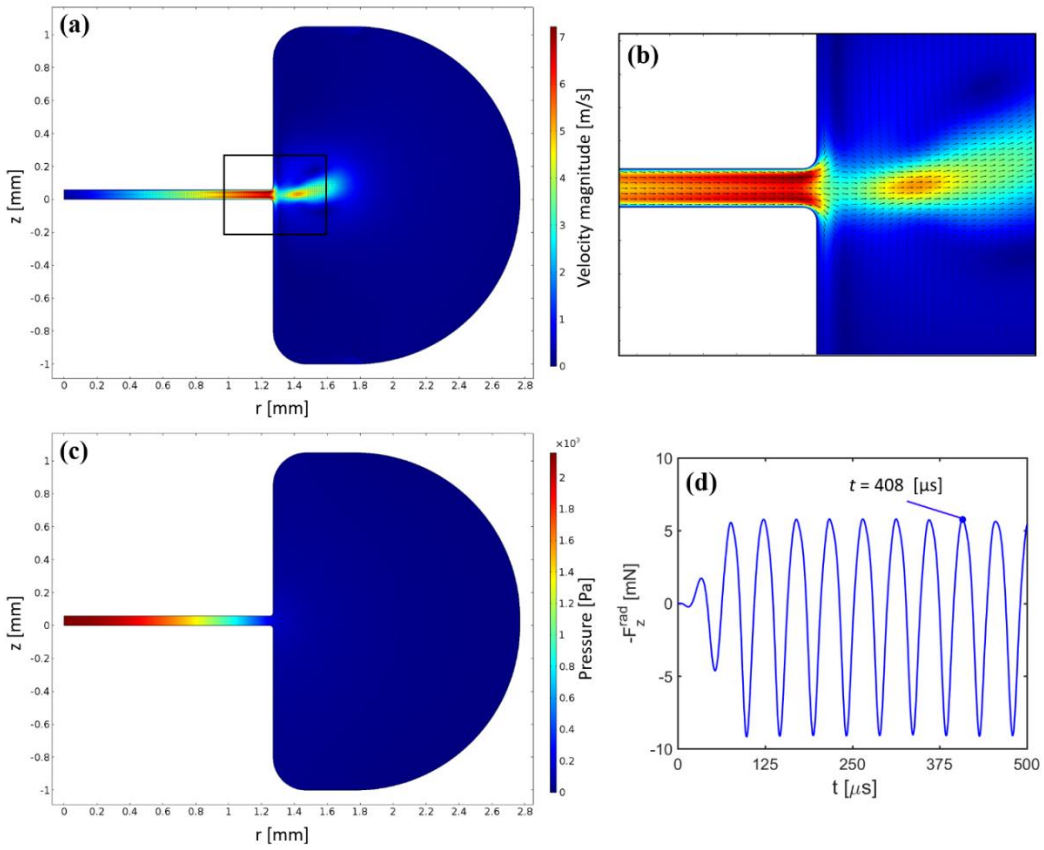

FIG. S6. Results obtained with CFD model for H = 50 µm. (a) Velocity field at t = 408 µs. (b) Zoom-in of the velocity field shown in (a). (c) Pressure field at t = 408 µs. (d) Vertical force on the object over time.

S3. Qualitative matching of experimental and simulated vertical forces

As shown in Fig. S7, there is a good qualitative agreement between the experimental and the simulated vertical force acting on an object. The differences between the numerical and experimental results may be caused by two main factors. On the one hand, the experimental force was measured on a rectangular object, whereas the axisymmetric CFD simulation employed a circular object of radius R = 1.27 mm due to the impossibility of executing a full 3D simulation. On the other hand, the accuracy of the experimental distance measurement was ±10 µm.

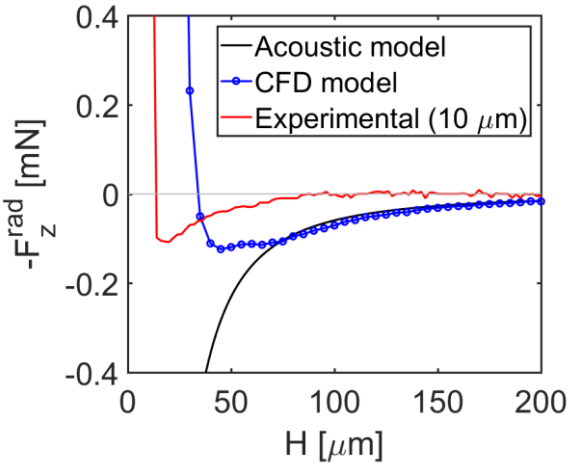

FIG. S7. Time-averaged vertical force exerted on the object as a function of the separation H obtained with the CFD model, the acoustic model and experimental measurements. The experimental results were measured on a SMD component with lateral dimensions of 1.6 mm x 3.2 mm. The results obtained with the acoustic model and the CFD model assumed a circular object of equivalent area (radius R = 1.27 mm).

S4. Effect of air viscosity on the transition from attractive to repulsive forces

We have conducted multiple CFD simulations to investigate the influence of air viscosity on the transition from repulsive to attractive forces. As we can observe in Fig. S8, the value of H (separation between the radiating tip and the object) at which the transition occurs increases with the air dynamic viscosity η. We present in Table S2 the comparison between the viscous penetration depth $\delta = \sqrt{2\eta/\rho_0\omega}$ and the values of H at which the transitions occurred.

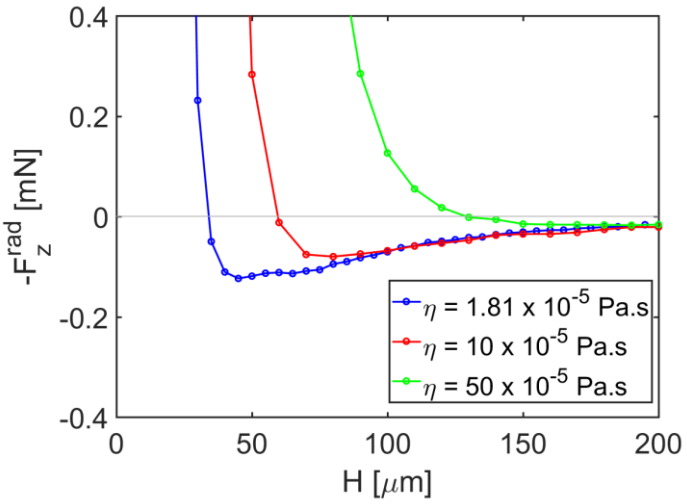

FIG. S8. Simulated vertical force exerted on a circular object of radius R = 1.27 mm for a transducer displacement amplitude of 10 μm, and different values of air dynamic viscosity η.

TABLE S2. Comparison between the viscous penetration depth δ and H (distance of force transition) for different air viscosities η.

η	H (transition)	δ
1.81 x 10^{-5} Pa.s	34 µs	15 µs
10 x 10^{-5} Pa.s	60 µs	35 µs
50 x 10^{-5} Pa.s	130 µs	79 µs

S5. Trapping of a non-flat object

Fig. S9 shows the trapping of an expanded polystyrene sphere of 7 mm in diameter. The sphere is levitated below the transducer without touching the vibrating tip.

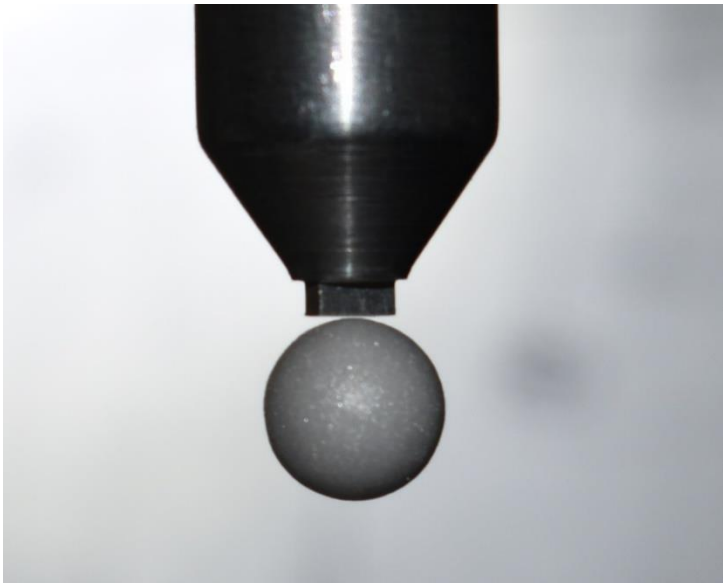

FIG. S9. Non-contact trapping of an expanded polystyrene sphere of 7 mm in diameter.